

Nuclear Constraints on $^{12}\text{C}(\alpha, \gamma)^{16}\text{O}$ and Their Impact on Black-Hole Mass Predictions

A. M. Mukhamedzhanov¹

¹*Texas A&M University, College Station, Texas 77843, USA*

Gravitational-wave observations have renewed interest in the black-hole mass gap and in the maximum mass of first-generation black holes below its lower edge. The $^{12}\text{C}(\alpha, \gamma)^{16}\text{O}$ reaction plays a central role in this problem because it determines the carbon-to-oxygen ratio after core-helium burning and thereby affects the later evolution of massive stars toward pulsational pair instability and pair-instability supernovae.

Recent attempts to constrain $S(300 \text{ keV})$ from gravitational-wave population inferences face important limitations, because the lower edge of the black-hole mass gap is not directly measured. It is inferred model dependently from assumptions about stellar evolution, metallicity, mass loss, rotation, binary evolution, hierarchical mergers, selection effects, priors, and the adopted population model. Therefore, values of $S(300 \text{ keV})$ inferred from black-hole populations must remain consistent with independent nuclear-physics constraints.

In this work we reanalyze the low-energy $^{12}\text{C}(\alpha, \gamma)^{16}\text{O}$ S factor using updated information on the subthreshold 1^- and 2^+ ANCs and on the ground-state ANC of ^{16}O , together with direct capture data. These constraints favor a lower $S(300 \text{ keV})$ than the older central evaluation and disfavor very large values required by some black-hole-population interpretations. Using the resulting ANC-constrained $S(300 \text{ keV})$ range and the transformed relation between this quantity and the lower edge of the pair-instability mass gap, we estimate

$$\frac{M_{\text{BH}}}{M_{\odot}} \simeq 61\text{--}75.$$

Thus, the present nuclear-physics constraints favor a relatively high lower edge of the first-generation black-hole mass gap.

I. INTRODUCTION

The reaction $^{12}\text{C}(\alpha, \gamma)^{16}\text{O}$ plays a central role in nuclear astrophysics because it determines the carbon-to-oxygen ratio established at the end of core-helium burning. Through its influence on the CO-core mass and on the subsequent susceptibility of massive stars to pulsational pair instability (PPI) and pair-instability supernova (PISN) evolution, this reaction also affects the maximum mass of first-generation black holes (BHs) below the pair-instability mass gap. Equivalently, it affects the lower edge of the pair-instability mass gap produced by stellar collapse. Recent gravitational-wave population studies have emphasized the search for the pair-instability black-hole mass gap, whose lower edge is commonly expected near 50–65 M_{\odot} . This has motivated attempts to connect the observed BH mass spectrum to the astrophysical factor $S(300 \text{ keV})$ for $^{12}\text{C}(\alpha, \gamma)^{16}\text{O}$ [1–7].

One of the most important studies in this context is Ref. [2]. Using

$$S(300 \text{ keV}) = 140 \pm 21 \text{ keV b}$$

from the evaluation of Ref. [8], Ref. [2] found that the lower edge of the pair-instability mass gap is shifted to about 64 M_{\odot} , while the upper edge is shifted to about 161 M_{\odot} . Rapid rotation can raise the lower edge further, to approximately 70 M_{\odot} . The relevance of this issue has increased because gravitational-wave observations have reported BHs with masses up to about 85 M_{\odot} , as well as numerous BHs in the 60–70 M_{\odot} range [9, 10]. More recently, Ref. [4] reported the discovery of new low-spin

BHs in the mass interval 50–70 M_{\odot} .

It is important to emphasize that gravitational-wave observations alone cannot uniquely determine the BH mass gap or the underlying BH mass spectrum. The inference depends on the adopted stellar-evolution model, including nuclear reaction rates, rotation, mass loss, Eddington-limited accretion, metallicity, and other initial conditions and parameters. Among the nuclear reactions that most strongly affect the BH mass spectrum are the triple- α reaction and $^{12}\text{C}(\alpha, \gamma)^{16}\text{O}$. The triple- α rate is often fixed by adopting the Caughlan–Fowler compilation [11]. The astrophysical factor $S(300 \text{ keV})$ for $^{12}\text{C}(\alpha, \gamma)^{16}\text{O}$, where 300 keV is the effective energy in the helium-burning Gamow window, has a particularly important influence on the predicted mass gap.

Regarding the role of $^{12}\text{C}(\alpha, \gamma)^{16}\text{O}$, we single out Refs. [1–3]. These works clearly demonstrated that the $^{12}\text{C}(\alpha, \gamma)^{16}\text{O}$ rate strongly influences the mass of the BH remnant formed in the collapse of a massive star and, therefore, the boundaries of the pair-instability mass gap. Depending on the adopted value of $S(300 \text{ keV})$, the lower edge of the gap can vary around $59_{-13}^{+34} M_{\odot}$, while the upper edge can vary around $139_{-14}^{+30} M_{\odot}$. These error bars were obtained by assigning a $\pm 3\sigma$ uncertainty to the $S(300 \text{ keV})$ factor for $^{12}\text{C}(\alpha, \gamma)^{16}\text{O}$. The physical reason is well understood. This reaction controls the post-helium-burning C/O ratio. A smaller $S(300 \text{ keV})$ leaves more residual carbon and therefore increases the C/O ratio, and helps the star avoid the PPI regime, thereby allowing a larger first-generation BH remnant. By contrast, a smaller post-helium-burning carbon abundance

weakens carbon burning and favors the onset of PPISN or PISN evolution, reducing the maximum BH mass or, in the case of full PISN, leaving no BH remnant.

Recently, Ref. [12] was accepted for publication. In that work, the pair-instability BH mass gap was shifted from 104–184 M_\odot down to approximately 45–135 M_\odot . This implies that the highest BH mass below the lower edge of the gap would be smaller than $\sim 45 M_\odot$. To support this conclusion, Ref. [12] appeals to the astrophysical inferences of Refs. [4–7].

However, these references do not all support such a low lower-edge mass cutoff. Ref. [7] obtained a lower-edge mass of $57_{-10}^{+17} M_\odot$, while Ref. [4] found a cutoff for low-spin BHs of $68_{-18.5}^{+19.8} M_\odot$ at the 90% credible level, consistent with $S(300 \text{ keV}) \simeq 110 \text{ keV b}$. Thus, the downward shift advocated in Ref. [12] is supported mainly by Refs. [5, 6], which suggest a lower-edge mass cutoff near 40–50 M_\odot .

This interpretation is problematic from the nuclear-physics point of view. As discussed in Ref. [7], the 99% credible intervals associated with Refs. [5, 6] correspond to $S(300 \text{ keV}) \simeq 150\text{--}450 \text{ keV b}$, which only marginally overlaps with the range recommended by Ref. [8], $S(300 \text{ keV}) \simeq 130\text{--}160 \text{ keV b}$. Similarly, the mass-gap shift in Ref. [12] to $\sim 45\text{--}135 M_\odot$ corresponds to $S(300 \text{ keV}) \simeq 138\text{--}263 \text{ keV b}$. The upper part of this interval is not compatible with contemporary nuclear-physics and nuclear-astrophysics constraints on $^{12}\text{C}(\alpha, \gamma)^{16}\text{O}$.

Agreement with astrophysical observables alone is therefore not sufficient. Any inference based on BH mass distributions must also remain consistent with independently established nuclear-physics constraints, including bounds on the ANCs and on the extrapolated S factor. A best fit or posterior maximum that lies outside the physically allowed nuclear domain is not a physically acceptable determination; it is only a mathematical compensation for missing, incomplete, or insufficiently constrained physics.

The purpose of the present work is to emphasize that any program aimed at determining BH masses and the black-hole mass gap can be physically meaningful only if the astrophysical inference is aligned with the independent nuclear constraints that govern the low-energy $^{12}\text{C}(\alpha, \gamma)^{16}\text{O}$ capture amplitude. Many studies pursuing this program have relied heavily on the state-of-the-art review by deBoer *et al.* [8], published in 2017. Since then, however, new results on the involved ANCs have become available that tend to shift the range

$$S(300 \text{ keV}) = 130\text{--}160 \text{ keV b}$$

from Ref. [8] toward lower values. A decrease of $S(300 \text{ keV})$ lowers the $^{12}\text{C}(\alpha, \gamma)^{16}\text{O}$ reaction rate, increases the maximum black-hole mass below the gap, and shifts the lower edge of the mass gap upward. These conclusions are based on new information about the asymptotic normalization coefficients (ANCs) that control the low-energy S factor. In what follows, we discuss this new

ANC information and its impact on black-hole masses below the lower edge of the pair-instability mass gap.

All calculations reported below were performed within the multilevel R -matrix formalism using the Brune parametrization, following the approach adopted in Ref. [8].

II. SUBTHRESHOLD AND GROUND-STATE ANCS

At low energies, the $^{12}\text{C}(\alpha, \gamma)^{16}\text{O}$ radiative-capture amplitude is dominated by the near-threshold subthreshold states of ^{16}O : the 1^- state at 7.12 MeV and the 2^+ state at 6.92 MeV. These states contribute through their subthreshold resonances, while additional contributions arise from resonances above threshold, direct capture (for $E2$), and smaller cascade transitions through bound excited states [13]. The subthreshold resonance contributions to the radiative capture arise through the long-range tails of their bound-state wave functions in the external region. The strengths of the subthreshold-resonance contributions are determined by the corresponding ANCs, C_1 and C_2 , determining the amplitudes of the overlap functions for the virtual decays $^{16}\text{O}(7.12 \text{ MeV}, 1^-)$ and $^{16}\text{O}(6.92 \text{ MeV}, 2^+)$, respectively. Together with the ground-state ANC $C_0 \equiv ^{16}\text{O}(0^+; 0.0 \text{ MeV})$, the subthreshold ANCs control the $S(300 \text{ keV})$ factor. Their quantitative contributions depend on the adopted ANC values. Table I of [14] presents a snapshot of the available experimental and theoretical ANC values.

There have been several important developments concerning the subthreshold and ground-state ANCs since the publication of Ref. [8]. First, these developments concern the subthreshold ANCs C_1 and C_2 . Low values of these ANCs were extracted from the sub-Coulomb transfer reaction



[15, 16]. These ANC determinations are regarded as among the most reliable currently available because the sub-Coulomb transfer reaction is practically insensitive to nuclear distortions in the initial and final channels. In addition, the Q value of the reaction is very small and the reaction is extremely peripheral. Therefore, no additional adjustable parameters, apart from the involved ANCs, are required to calculate the sub-Coulomb transfer differential cross section. The differential cross section is proportional to

$$\frac{d\sigma}{d\Omega} \propto C_\alpha^2 C_{^{12}\text{C}}^2 C_{\alpha d}^2.$$

In Refs. [15, 16], the extraction of C_1 and C_2 used the ^6Li ANC

$$C_{\alpha d} = 5.3 \pm 0.5 \text{ fm}^{-1/2}$$

from Ref. [17].

The subthreshold ANCs extracted from the sub-Coulomb transfer reaction (1),

$$C_1 = 2.08 \times 10^{14} \text{ fm}^{-1/2}, \quad C_2 = 1.14 \times 10^5 \text{ fm}^{-1/2},$$

were regarded as among the most reliable and were adopted in Ref. [8] for the R -matrix analysis of the $^{12}\text{C}(\alpha, \gamma)^{16}\text{O}$ reaction.

More recently, *ab initio* no-core shell-model-with-continuum calculations revised the value of $C_{\alpha d}^2$ upward by about 30% [18],

$$C_{\alpha d}^2 = 6.864 \pm 0.210 \text{ fm}^{-1},$$

which implies a reduction of about 14% in the deduced values of C_1 and C_2 . The revised ANCs become

$$\begin{aligned} C_1 &= (1.83 \pm 0.08) \times 10^{14} \text{ fm}^{-1/2}, \\ C_2 &= (0.98 \pm 0.08) \times 10^5 \text{ fm}^{-1/2}. \end{aligned} \quad (2)$$

These revised values are significantly lower than those adopted in Ref. [8] and therefore tend to reduce the extrapolated low-energy $E1$ and $E2$ contributions. Since the capture through a subthreshold state is proportional to C_s^2 ($C_s = C_1, C_2$), the reduction of the subthreshold C_s^2 values implies a comparable reduction in the corresponding subthreshold contribution to $S(300 \text{ keV})$.

Note that recently determined subthreshold ANCs obtained by extrapolating elastic-scattering phase shifts to the corresponding bound-state poles [19], $C_1 = (1.42 \pm 0.05) \times 10^{14} \text{ fm}^{-1/2}$ and $C_2 = (2.27 \pm 0.02) \times 10^5 \text{ fm}^{-1/2}$ lie near the upper end of the adopted range of subthreshold ANCs. However, their accuracy is limited by the uncertainties in the elastic-scattering phase shifts, although the extrapolation method itself is model independent.

The most significant change in the ANC landscape since the evaluation of Ref. [8] concerns the ground-state ANC C_0 . As summarized in Table I, all recent studies included in the present comparison give values

$$C_0 \gtrsim 600 \text{ fm}^{-1/2},$$

in contrast to the value

$$C_0 = 58 \text{ fm}^{-1/2}$$

adopted in Ref. [8]. This change has important consequences for the external-capture contribution to the ground-state transition and therefore for the extrapolated S factor at astrophysical energies.

III. BAYESIAN CONSTRAINT ON C_0 FROM THE $E2$ COMPONENT

The direct $E1$ transition to the ground state of ^{16}O in the reaction $^{12}\text{C}(\alpha, \gamma)^{16}\text{O}$ is strongly suppressed because it is isospin forbidden. Consequently, the direct $E1$

external-capture contribution to the ground-state transition is negligible. The $E1$ contribution is therefore governed mainly by the resonant and subthreshold 1^- amplitudes and does not provide a useful direct constraint on the ground-state ANC C_0 . For this reason, in selecting the most probable value of C_0 , we begin with the $E2$ component, where the external-capture contribution to the ground-state transition is more directly connected with C_0 .

Guided by the available experimental information summarized in Table I, we perform a Bayesian analysis using a flat prior in the interval

$$600 \leq C_0 \leq 900 \text{ fm}^{-1/2}.$$

The extracted S_{E2} data of Ref. [20] are used to constrain C_0 , while the subthreshold 2^+ ANC is kept fixed at the value favored by the sub-Coulomb transfer analysis, see Eq. (2). This is an important constraint because C_2 controls the strength of the subthreshold 2^+ contribution and the associated interference pattern in the $E2$ capture amplitude.

In contrast, the dependence on the ground-state ANC C_0 is weaker. This is because the dominant $E2$ contribution at low energy arises mainly from the interference between the subthreshold 2^+ resonance and the direct-capture amplitude to the ground state. The ground-state ANC C_0 enters primarily through the normalization of this external direct-capture amplitude and therefore has a less pronounced effect than the subthreshold ANC C_2 .

For each selected value of C_0 , the $E2$ capture calculation was repeated and compared with the extracted S_{E2} data. The likelihood was taken in the Gaussian form,

$$\mathcal{L}(D_{E2}|C_0) \propto \exp \left[-\frac{1}{2} \chi_{E2}^2(C_0) \right],$$

where

$$\chi_{E2}^2(C_0) = \sum_i \left[\frac{S_{E2}^{\text{th}}(E_i; C_0, C_2) - S_{E2,i}^{\text{exp}}}{\sigma_i} \right]^2.$$

Here D_{E2} denotes the set of extracted $E2$ data points used in the fit. The quantity $\mathcal{L}(D_{E2}|C_0)$ is the likelihood function, which measures how well a given value of C_0 reproduces the data D_{E2} . The theoretical value $S_{E2}^{\text{th}}(E_i; C_0, C_2)$ is the calculated $E2$ astrophysical S factor at the experimental energy E_i , obtained with the trial value of C_0 and the fixed subthreshold ANC C_2 . The quantity $S_{E2,i}^{\text{exp}}$ is the corresponding experimentally extracted $E2$ astrophysical S factor, and σ_i is its quoted experimental uncertainty.

Thus, each term in the sum is the squared residual between theory and experiment, measured in units of the experimental error. The exponential form of the likelihood follows from assuming Gaussian, uncorrelated experimental uncertainties. Under this assumption, smaller values of $\chi_{E2}^2(C_0)$ correspond to larger likelihoods and therefore to larger posterior probabilities.

TABLE I. ANC values C_0 for the overlap $^{16}\text{O}(\text{g.s.}) \rightarrow \alpha + ^{12}\text{C}(\text{g.s.})$. For Ref. [21], three values of C_0 were obtained using three different interaction potentials.

ANC	Ref. [22]	Ref. [23]	Ref. [24]	Ref. [25]	Ref. [21]	Ref. [26]
C_0 ($\text{fm}^{-1/2}$)	709	744 ± 144	740	637 ± 86	3390; 1230; 790	837–841

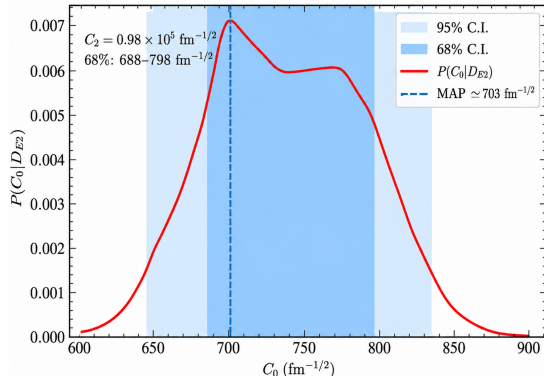


FIG. 1. Smoothed Bayesian posterior distribution for the ground-state ANC C_0 , obtained from the extracted S_{E2} data with the subthreshold 2^+ ANC fixed at $C_2 = 0.98 \times 10^5 \text{ fm}^{-1/2}$. A flat prior was used over the interval $600 \leq C_0 \leq 900 \text{ fm}^{-1/2}$. The posterior peaks at $C_0^{\text{MAP}} \simeq 703 \text{ fm}^{-1/2}$, while the posterior median is $C_0^{\text{med}} \simeq 740 \text{ fm}^{-1/2}$. The shaded regions denote the 68% and 95% credible intervals, $688 \leq C_0 \leq 798 \text{ fm}^{-1/2}$ and $645 \leq C_0 \leq 840 \text{ fm}^{-1/2}$, respectively.

The flat prior is

$$\pi(C_0) = \begin{cases} \text{const}, & 600 \leq C_0 \leq 900 \text{ fm}^{-1/2}, \\ 0, & \text{otherwise.} \end{cases}$$

The posterior distribution is then

$$P(C_0|D_{E2}) = \frac{\mathcal{L}(D_{E2}|C_0) \pi(C_0)}{\int \mathcal{L}(D_{E2}|C_0) \pi(C_0) dC_0}.$$

Equivalently, for numerical stability, we evaluate

$$P(C_0|D_{E2}) \propto \exp \left[-\frac{1}{2} (\chi_{E2}^2(C_0) - \chi_{E2,\min}^2) \right],$$

inside the prior interval. Here $\chi_{E2,\min}^2$ denotes the minimum value of $\chi_{E2}^2(C_0)$ obtained within the scanned prior interval. Thus

$$\chi_{E2}^2(C_0) - \chi_{E2,\min}^2 \equiv \Delta\chi_{E2}^2(C_0),$$

and the subtraction only rescales the likelihood by a constant factor without changing the posterior shape.

The resulting posterior distribution is shown in Fig. 1¹

¹ The vertical axis shows the posterior probability density, not

The maximum of the posterior, or MAP value, occurs at $C_0^{\text{MAP}} = 703 \text{ fm}^{-1/2}$. The median value is $C_0^{\text{med}} \simeq 740 \text{ fm}^{-1/2}$, and the credible intervals are

$$688 \leq C_0 \leq 798 \text{ fm}^{-1/2} \quad (68\%),$$

and

$$645 \leq C_0 \leq 840 \text{ fm}^{-1/2} \quad (95\%).$$

Thus the Bayesian analysis favors the same range of C_0 values indicated by recent ANC determinations summarized in Table I.²

The corresponding $E2$ contribution at $E = 300 \text{ keV}$ is approximately $S_{E2}(300 \text{ keV}) = 50 \text{ keV b}$ for $C_0^{\text{med}} = 740 \text{ fm}^{-1/2}$, and $S_{E2}(300 \text{ keV}) = 49 \text{ keV b}$ for the posterior maximum, $C_0^{\text{MAP}} = 703 \text{ fm}^{-1/2}$. Over the main posterior region the variation of $S_{E2}(300 \text{ keV})$ with C_0 is very modest. For example, increasing C_0 from 740 to 870 $\text{fm}^{-1/2}$ changes $S_{E2}(300 \text{ keV})$ only by a few keV b. This confirms that the low-energy $E2$ extrapolation is more sensitive to the subthreshold ANC C_2 and to the interference pattern than to moderate variations of C_0 .

The posterior also provides a useful lower-side constraint. When the scan was extended below the prior interval, the case $C_0 = 550 \text{ fm}^{-1/2}$ gave a substantially worse description of the extracted S_{E2} data. The best interference branch for $C_0 = 550 \text{ fm}^{-1/2}$ yielded

$$\chi_{E2}^2 = 22.13, \quad \chi_{\nu,E2}^2 = 2.77,$$

compared with

$$\chi_{E2}^2 \simeq 5.8, \quad \chi_{\nu,E2}^2 \simeq 0.73,$$

near the preferred region around $C_0^{\text{MAP}} = 703 \text{ fm}^{-1/2}$. For the median value $C_0^{\text{med}} = 740 \text{ fm}^{-1/2}$, we find

$$\chi_{\nu,E2}^2 \simeq 0.78.$$

Therefore, the S_{E2} -only data do not favor a drift toward very low values of the ground-state ANC.

We emphasize that the S_{E2} -only posterior is used as the cleaner Bayesian diagnostic for the $E2$ extrapolation, while the total-capture comparison serves as a consistency test of the complete $E1 + E2$ +cascade model.

the probability itself. The density is normalized according to $\int_{600}^{900} P(C_0|D_{E2}) dC_0 = 1$. Since C_0 is measured in $\text{fm}^{-1/2}$ and the posterior extends over a range of order $10^2 \text{ fm}^{-1/2}$, density values of order 10^{-3} – 10^{-2} are expected.

² We do not include the result of Ref. [27], which reported $C_0 = 337 \pm 45 \text{ fm}^{-1/2}$, because it lies outside the 95% credible interval obtained in the present S_{E2} -only Bayesian analysis and is also in tension with the other recent determinations listed in Table I.

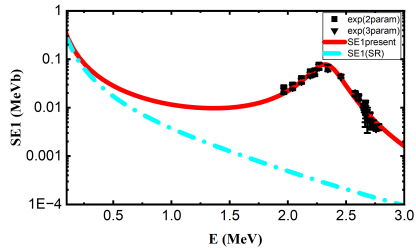


FIG. 2. The $S_{E1}(E)$ factor obtained from the R -matrix analysis, compared with the experimental two-parameter and three-parameter data of Ref. [20]. The black rectangles are the two-parameter data, and the inverted black triangles are the three-parameter data. The red solid line is the best R -matrix fit. The green dash-dotted line is the contribution from the 1^- subthreshold resonance.

IV. COMPARISON WITH EXPERIMENTAL DATA

We present here the comparison of the three-level R -matrix calculations for the $E1$ and $E2$ radiative transitions in the $^{12}\text{C}(\alpha, \gamma)^{16}\text{O}$ reaction. As discussed above, for this comparison we use the extracted $E1$ and $E2$ multipole data of Ref. [20]. We adopt

$$C_1 = 1.83 \times 10^{14} \text{ fm}^{-1/2}, \quad C_2 = 0.98 \times 10^5 \text{ fm}^{-1/2},$$

which are the most reliable latest subthreshold ANCs, and the posterior median value

$$C_0^{\text{med}} = 740 \text{ fm}^{-1/2}$$

obtained from the Bayesian analysis. These values are used in the following calculations.

In Figs. 2 and 3, the calculated and experimental S factors are shown. The adopted fitting parameters are listed in Tables II and III. The calculated S factors were fitted to the experimental multipole data using the multilevel R -matrix approach following Ref. [8].

In both figures the red solid lines are the calculated total S_{E1} and S_{E2} factors, while the green dash-dotted curves show the contributions from the subthreshold resonances, 1^- for $E1$ and 2^+ for $E2$. These contributions are governed by the corresponding subthreshold ANCs and give significant fractions of the total $S_{E1}(300 \text{ keV})$ and $S_{E2}(300 \text{ keV})$ factors, as summarized in Tables IV and V. Figures 2 and 3 illustrate why the subthreshold ANCs C_1 and C_2 play a pivotal role in determining $S_{E1}(300 \text{ keV})$ and $S_{E2}(300 \text{ keV})$, respectively.

The fit for the $E1$ transition is more straightforward than for $E2$, because the direct $E1$ transition to the ground state is negligible and S_{E1} is practically insensitive to the value of C_0 . The dominant contribution

TABLE II. Definitions of the parameters adopted in the R -matrix fit for the $E1$ transition.

Parameter	Description
$r_0 = 5.43 \text{ fm}$	Channel radius used in the R -matrix calculation.
$\epsilon_{s1} = 0.045 \text{ MeV}$	Binding energy of the 1^- subthreshold state relative to the $\alpha + ^{12}\text{C}$ threshold.
$E_{s1} = -0.045 \text{ MeV}$	Energy of the 1^- subthreshold state measured relative to the $\alpha + ^{12}\text{C}$ threshold.
$\epsilon_0 = 7.162 \text{ MeV}$	Binding energy of the ^{16}O ground state relative to the $\alpha + ^{12}\text{C}$ threshold.
$E_{R1} = 2.423 \text{ MeV}$	Resonance energy of the first above-threshold 1^- state.
$E_{RBG} = 10.5 \text{ MeV}$	Energy of the background 1^- resonance.
$C_0 = 740 \text{ fm}^{-1/2}$	ANC of the ^{16}O ground state.
$C_1 = 1.83 \times 10^{14} \text{ fm}^{-1/2}$	ANC of the 1^- subthreshold state.
$\Gamma_{R1} = 0.50 \text{ MeV}$	Particle width of the first above-threshold 1^- resonance.
$\Gamma_{RBG} = 1.0 \text{ MeV}$	Particle width of the background 1^- resonance.
$\Gamma_{\gamma 0} = 55 \times 10^{-9} \text{ MeV}$	Radiative width of the 1^- subthreshold state for the transition to the ground state.
$\Gamma_{\gamma R1} = 19 \times 10^{-9} \text{ MeV}$	Radiative width of the first above-threshold 1^- resonance for the transition to the ground state.
$\Gamma_{\gamma BG0} = 1.4 \times 10^{-6} \text{ MeV}$	Radiative width of the background 1^- resonance for the transition to the ground state.
$L = 1$	Electromagnetic multipolarity of the $E1$ transition.
$\ell_i = 1$	Initial-channel orbital angular momentum.
$\ell_f = 0$	Final bound-state orbital angular momentum for the ground-state transition.
$J_i = 1$	Spin of the initial 1^- state.
$J_f = 0$	Spin of the final ground state of ^{16}O .

to $S_{E1}(300 \text{ keV})$ comes from the subthreshold 1^- state and the above-threshold 1^- resonance at $E_{R1} = 2.423 \text{ MeV}$. To fit the experimental $E1$ data of Ref. [20], we adopted a three-level R -matrix model including the subthreshold 1^- state at $E_{s1} = -0.045 \text{ MeV}$, the resonance at $E_{R1} = 2.423 \text{ MeV}$, and a background resonance. As in Ref. [8], the subthreshold state and the 2.423 MeV resonance interfere constructively. The background resonance contributes mainly at higher energies and does not affect the low-energy behavior near 300 keV. The best fit

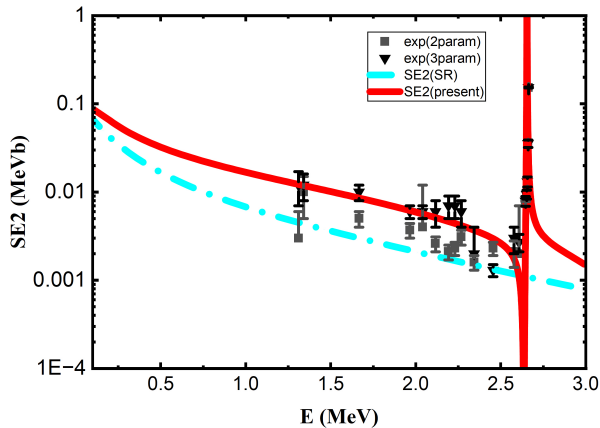


FIG. 3. The $S_{E2}(E)$ factor obtained from the R -matrix analysis, compared with the experimental two-parameter and three-parameter data of Ref. [20]. The notation is the same as in Fig. 2, except that the green dash-dotted line shows the contribution from the 2^+ subthreshold resonance.

gives

$$S_{E1}(300 \text{ keV}) = 62 \text{ keV b}$$

with reduced chi-squares $\chi_\nu^2 = 1.35$ for the two-parameter data set and $\chi_\nu^2 = 1.15$ for the three-parameter data set.

The fit for the $E2$ transition is more delicate. To fit the $E2$ data of Ref. [20], we used, as in Ref. [8], a three-level R -matrix model containing the subthreshold 2^+ state, the narrow 2^+ resonance at $E_{R1} = 2.654$ MeV, and the broader 2^+ resonance at $E_{R2} = 4.344$ MeV. The dominant low-energy contribution to $S_{E2}(300 \text{ keV})$ comes from the subthreshold 2^+ state and from direct capture to the ^{16}O ground state.

The large value $C_0 = 740 \text{ fm}^{-1/2}$ significantly complicates the $E2$ fit. In Ref. [8], the combination $C_2 = 1.14 \times 10^5 \text{ fm}^{-1/2}$ and the much smaller $C_0 = 58 \text{ fm}^{-1/2}$ favored destructive interference between the subthreshold 2^+ amplitude and the direct-capture amplitude to the ground state. In contrast, when the larger modern value of C_0 is adopted together with the lower subthreshold ANC C_2 , the fit requires constructive interference between the subthreshold and direct capture amplitudes. With this choice, we obtain a good description of the three-parameter $E2$ data of Ref. [20]; the two-parameter data lie systematically lower and are not fitted simultaneously. The best fit has $\chi_\nu^2 = 0.78$, and gives $S_{E2}(300 \text{ keV}) = 50 \text{ keV b}$. In evaluating χ_ν^2 , we excluded the narrow-resonance region around E_{R1} and the point at $E = 2.455$ MeV, which lies visibly below the surrounding data and has a very small uncertainty, thereby driving the total χ_ν^2 to an unrealistically large value. The parameter set of Ref. [8] also gives a good fit, with $\chi_\nu^2 = 0.96$ and

$$S_{E2}(300 \text{ keV}) = 51 \text{ keV b}.$$

TABLE III. Definitions of the parameters adopted in the R -matrix fit for the $E2$ transition.

Parameter	Description
$r_0 = 5.43 \text{ fm}$	Channel radius used in the R -matrix calculation.
$\epsilon_{s2} = 0.2449 \text{ MeV}$	Binding energy of the 2^+ subthreshold state relative to the $\alpha + ^{12}\text{C}$ threshold.
$E_{s2} = -0.2449 \text{ MeV}$	Energy of the 2^+ subthreshold state measured relative to the $\alpha + ^{12}\text{C}$ threshold.
$\epsilon_0 = 7.162 \text{ MeV}$	Binding energy of the ^{16}O ground state relative to the $\alpha + ^{12}\text{C}$ threshold.
$E_{R1} = 2.654 \text{ MeV}$	Resonance energy of the first above-threshold 2^+ state.
$E_{R2} = 4.344 \text{ MeV}$	Resonance energy of the second above-threshold 2^+ state.
$C_0 = 740 \text{ fm}^{-1/2}$	ANC of the ^{16}O ground state.
$C_2 = 0.98 \times 10^5 \text{ fm}^{-1/2}$	ANC of the 2^+ subthreshold state.
$\Gamma_{R1} = 6.2 \times 10^{-4} \text{ MeV}$	Particle width of the first above-threshold 2^+ resonance.
$\Gamma_{R2} = 0.12 \text{ MeV}$	Particle width of the second above-threshold 2^+ resonance.
$\Gamma_{\gamma 0} = 9.7 \times 10^{-8} \text{ MeV}$	Radiative width of the 2^+ subthreshold state for the transition to the ground state.
$\Gamma_{\gamma R1} = 5 \times 10^{-9} \text{ MeV}$	Radiative width of the first above-threshold 2^+ resonance for the transition to the ground state.
$\Gamma_{\gamma R2} = 6.2 \times 10^{-7} \text{ MeV}$	Radiative width of the second above-threshold 2^+ resonance for the transition to the ground state.
$L = 2$	Electromagnetic multipolarity of the $E2$ transition.
$\ell_i = 2$	Initial-channel orbital angular momentum for the $E2$ transition.
$\ell_f = 0$	Final bound-state orbital angular momentum for the ground-state transition.
$J_i = 2$	Spin of the initial 2^+ state.
$J_f = 0$	Spin of the final ground state of ^{16}O .

Table IV displays two ANC sets used in the calculations. Set 1 is the present choice, based on the updated subthreshold ANCs and the Bayesian median value adopted for the modern large ground-state ANC C_0 . Set 2 keeps the original subthreshold ANCs of Refs. [15, 16], as used in Ref. [8], but adopts the same large value $C_0 = 740 \text{ fm}^{-1/2}$. This comparison isolates the effect of the subthreshold ANCs at fixed C_0 .

The effect of changing the subthreshold ANCs is much larger than the effect of moderate variations of C_0 . The contribution of the subthreshold 1^- state to the total $E1$ S factor at 300 keV is about 71–74%. The re-

TABLE IV. ANC sets used in the calculations summarized in Table V.

Set	C_1 ($\text{fm}^{-1/2}$)	C_2 ($\text{fm}^{-1/2}$)	C_0 ($\text{fm}^{-1/2}$)
1	1.83×10^{14}	0.98×10^5	740
2	2.08×10^{14}	1.14×10^5	740

TABLE V. The $S(300 \text{ keV})$ factors for the radiative capture reaction $^{12}\text{C}(\alpha, \gamma)^{16}\text{O}$. Here S_{E1} and S_{E2} are the total S factors for the $E1$ and $E2$ transitions, respectively, and $S_{\text{tot}} = S_{E1} + S_{E2}$. The quantities $S_{E1}^{(\text{SR})}$ and $S_{E2}^{(\text{SR})}$ denote the subthreshold-resonance contributions at 300 keV. All S factors are in keV b. Cascade transitions are not included.

Set	S_{E1}	S_{E2}	S_{tot}	$S_{E1}^{(\text{SR})}$	$S_{E2}^{(\text{SR})}$	$\frac{S_{E1}^{(\text{SR})}}{S_{E1}}$	$\frac{S_{E2}^{(\text{SR})}}{S_{E2}}$
1	62	50	112	46	30	0.74	0.60
2	85	58	143	60	46	0.71	0.79

maining contribution comes mainly from interference between the subthreshold 1^- state and the broad 1^- resonance at $E_x = 9.585 \text{ MeV}$. The direct $E1$ capture contribution to the ground state is negligible even for $C_0 = 740 \text{ fm}^{-1/2}$. For the $E2$ transition, the constructive interference required by the fit between the subthreshold resonance and direct-capture amplitudes increases $S_{E2}(300 \text{ keV})$ compared with the pure subthreshold contribution $S_{E2}^{(\text{SR})}(300 \text{ keV})$. The renormalized subthreshold ANC of Ref. [18] reduce both $S_{E1}^{(\text{SR})}(300 \text{ keV})$ and $S_{E2}^{(\text{SR})}(300 \text{ keV})$ by about 30% compared with the values obtained using the original subthreshold ANCs of Refs. [15, 16]. Consequently, the ANC update decreases the total low-energy S factor.

Having established the impact of the updated subthreshold ANCs and the large ground-state ANC on the $E1$ and $E2$ transitions, we now consider the total S factor,

$$S_{\text{tot}}(E) = S_{E1}(E) + S_{E2}(E) + S_{\text{casc}}(E),$$

where $S_{\text{casc}}(E)$ is the cascade contribution. The $S_{E1}(E)$ and $S_{E2}(E)$ contributions are taken from the fits to the data of Ref. [20], while the cascade contribution is taken from Ref. [8].

The calculated $S_{\text{tot}}(E)$ is compared with the total-capture data of Refs. [28, 29]. The data from Ref. [28] are supplemented by the two low-energy total S -factor points at $E = 1.2$ and 1.5 MeV from Ref. [29]. The result is shown in Fig. 4.

The ANCs of the subthreshold 1^- and 2^+ states, the ground-state ANC, and the available low-energy total data, especially the points of Ref. [29], impose strong restrictions on the physically acceptable range of $S(300 \text{ keV})$.

It is important to distinguish between the quality of the separate multipole fits and the quality of the comparison

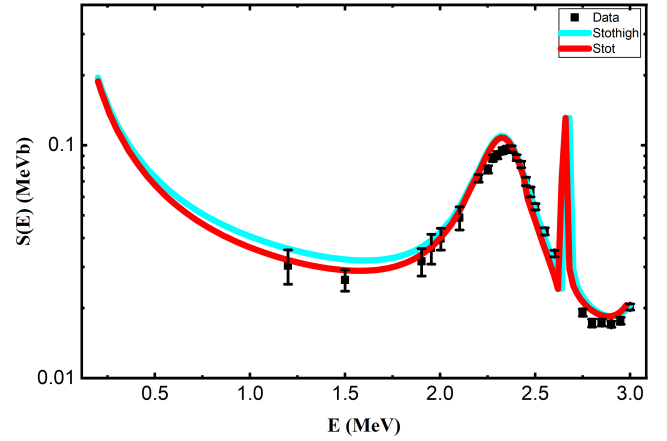


FIG. 4. The total $S_{\text{tot}}(E)$ factor obtained from the present $E1$ and $E2$ fits. The red solid line is obtained by summing the red solid curves in Figs. 2 and 3, together with the cascade contribution. It corresponds to $C_1 = 1.83 \times 10^{14} \text{ fm}^{-1/2}$, $C_2 = 0.98 \times 10^5 \text{ fm}^{-1/2}$, and $C_0 = 740 \text{ fm}^{-1/2}$. For comparison, the green solid line shows the result obtained with $C_0 = 900 \text{ fm}^{-1/2}$.

with the total-capture data. The $E1$ and $E2$ contributions were adjusted and tested against the corresponding extracted multipole data of Ref. [20]. In that comparison, the individual calculated multipole curves provide a very good description of the data. The total S -factor comparison, however, involves a different experimental situation. It combines the calculated $E1$, $E2$, and cascade contributions and compares their sum with total-capture data from Ref. [28] and with the two low-energy total points of Ref. [29].

Therefore, one cannot expect a perfect fit to the total data of Refs. [28, 29]. These measurements may have different absolute normalizations, quoted uncertainties, systematic effects, and correlations from those entering the extracted multipole data of Ref. [20]. Consequently, the total comparison should be viewed as a consistency test of the complete $E1+E2$ +cascade calculation rather than as a direct refit of the individual multipole components. Nevertheless, the calculated total S factor obtained from the multipole fits to the data of Ref. [20] shows good overall agreement with the independent total-capture data of Refs. [28, 29].

For the adopted ANC values $C_1 = 1.83 \times 10^{14} \text{ fm}^{-1/2}$, $C_2 = 0.98 \times 10^5 \text{ fm}^{-1/2}$, and the posterior median value $C_0^{\text{med}} = 740 \text{ fm}^{-1/2}$, we obtain

$$S_{\text{tot}}(300 \text{ keV}) = 118 \text{ keV b.}$$

Propagating the S_{E2} -only posterior for C_0 , with

$$688 \leq C_0 \leq 798 \text{ fm}^{-1/2} \quad (68\% \text{ credible interval}),$$

gives the corresponding range

$$S_{\text{tot}}(300 \text{ keV}) \simeq 116\text{--}119 \text{ keV b} \quad (3)$$

Thus, the Bayesian inference strongly constrains the uncertainty in $S_{\text{tot}}(300 \text{ keV})$ associated with the uncertainty in C_0 .

In addition to the uncertainty caused by C_0 , one must also account for the more sensitive uncertainties associated with the subthreshold ANCs C_1 and C_2 . According to Ref. [18], $C_1 = (1.83\text{--}1.84) \times 10^{14} \text{ fm}^{-1/2}$ and $C_2 = (0.98\text{--}1.07) \times 10^5 \text{ fm}^{-1/2}$. These ranges give

$$S_{E1}(300 \text{ keV}) = 62\text{--}63 \text{ keV b}, \quad (4)$$

and

$$S_{E2}(300 \text{ keV}) = 50\text{--}54 \text{ keV b}. \quad (5)$$

Thus, before adding the cascade contribution,

$$S_{E1}(300 \text{ keV}) + S_{E2}(300 \text{ keV}) = 112\text{--}117 \text{ keV b}.$$

After including the fixed cascade contribution, this corresponds to

$$S_{\text{tot}}(300 \text{ keV}) = 117\text{--}122 \text{ keV b}.$$

Taking the envelope of the ANC-driven uncertainties from both the C_0 posterior and the adopted C_1 , C_2 ranges, we obtain

$$S_{\text{tot}}(300 \text{ keV}) \simeq 116\text{--}122 \text{ keV b}.$$

Equivalently, for the central value

$$S_{\text{tot}}(300 \text{ keV}) \simeq 118 \text{ keV b},$$

this may be written as

$$S_{\text{tot}}(300 \text{ keV}) = 118_{-2}^{+4} \text{ keV b}.$$

Here the quoted uncertainty reflects the propagated ANCs uncertainty only; it does not include additional possible systematic uncertainties from the choice of R -matrix parametrization, channel radius, higher-lying levels, or experimental normalization effects.

If all these additional uncertainties are included, the total error band should be larger than the ANC-driven range quoted above. A conservative estimate can be obtained by adopting a relative uncertainty comparable to that of the deBoer *et al.* [8], and applying the same relative uncertainty to our central value $S_{\text{tot}}(300 \text{ keV}) = 118 \text{ keV b}$, gives

$$\Delta S_{\text{tot}} \simeq 118 \frac{20}{140} \simeq 17 \text{ keV b}.$$

Thus, as a conservative systematic estimate, one may write

$$S_{\text{tot}}(300 \text{ keV}) \simeq 118 \pm 17 \text{ keV b}. \quad (6)$$

This broader uncertainty should be interpreted as an approximate systematic scale rather than as the Bayesian uncertainty obtained from the C_0 posterior alone.

The main conclusion is that the latest updates of the subthreshold and ground-state ANCs push $S(300 \text{ keV})$ noticeably downward compared with the value obtained in Ref. [8].

V. PHYSICAL RELATION BETWEEN $S(300 \text{ keV})$ AND THE LOWER EDGE OF THE BLACK-HOLE MASS GAP

From the standpoint of stellar-evolution physics, the relation between the lower edge of the first-generation BH mass gap and $S(300 \text{ keV})$ should be inverse. Increasing the $^{12}\text{C}(\alpha, \gamma)^{16}\text{O}$ rate enhances the conversion of ^{12}C into ^{16}O during core-helium burning and therefore leaves a smaller residual carbon abundance at helium exhaustion. A smaller post-helium-burning carbon abundance weakens subsequent shell-carbon burning, reduces its stabilizing effect on the core, and promotes an earlier onset of pulsational pair-instability episodes or a full pair-instability supernova behavior. Consequently, increasing $S(300 \text{ keV})$ should lower, rather than raise, the maximum mass of a first-generation BH. Equivalently, larger values of $S(300 \text{ keV})$ should correspond to a smaller lower edge of the black-hole mass gap.

This inverse trend is physically natural and must remain the basis of any consistent interpretation of gravitational-wave data. If very large values of $S(300 \text{ keV})$ shift the lower edge of the pair-instability mass gap down to $\sim 40\text{--}50 M_{\odot}$, then BHs observed in the $50\text{--}70 M_{\odot}$ range would lie inside the predicted gap rather than below it. Therefore, if very large values of $S(300 \text{ keV})$ shift the lower edge of the pair-instability mass gap down to $\sim 40\text{--}50 M_{\odot}$, then BHs observed in the $50\text{--}70 M_{\odot}$ range would lie inside the predicted gap rather than below it.

This difficulty is not only astrophysical. Very large inferred values of $S(300 \text{ keV})$, required to push the lower edge of the mass gap down to $\sim 40\text{--}50 M_{\odot}$, are also incompatible with the experimental nuclear data for $^{12}\text{C}(\alpha, \gamma)^{16}\text{O}$ and with contemporary ANC measurements. Agreement with a population-level gravitational-wave inference alone is therefore insufficient; the inferred reaction rate must also satisfy the independent nuclear-physics constraints.

It is important to emphasize that the lower edge of the black-hole mass gap is not directly measured. It is inferred from the observed black-hole population, and the result depends on the assumptions made in the analysis. These assumptions include how many BHs may come from hierarchical mergers, what spin and mass distributions are used, how observational selection effects are treated, and what population model is adopted.

For this reason, different studies do not always determine the same quantity. Some analyses find evidence for BHs in the $50\text{--}70 M_{\odot}$ range and therefore favor a higher lower edge of the gap. Other analyses allow a lower edge near $40\text{--}50 M_{\odot}$, but this conclusion depends strongly on the chosen population model and on how second-generation BHs are treated. Thus these results should not be regarded as direct measurements of one unique, well-defined lower edge of the first-generation pair-instability mass gap.

Thus, purely astrophysical population inferences from

current gravitational-wave data do not robustly determine the lower edge of the black-hole mass gap in a model-independent way. Independent nuclear-physics information must be included from the outset.

The essential nuclear inputs for determining the maximum mass of first-generation BHs, and hence the lower edge of the pair-instability mass gap, include the triple- α reaction rate, the $^{12}\text{C} + ^{12}\text{C}$ fusion rate, and the $^{12}\text{C}(\alpha, \gamma)^{16}\text{O}$ reaction rate at astrophysically relevant temperatures. The triple-alpha reaction first produces the ^{12}C nuclei during helium burning. These carbon nuclei then serve as the target for the subsequent $^{12}\text{C}(\alpha, \gamma)^{16}\text{O}$ reaction, which converts part of the newly formed carbon into oxygen. The reaction rate for the triple-alpha process was adopted from Ref. [11].

The role of later carbon and oxygen burning should also be kept in perspective. Work [1] considered variations of the triple-alpha reaction, $^{12}\text{C}(\alpha, \gamma)^{16}\text{O}$, $^{12}\text{C} + ^{12}\text{C}$, and $^{16}\text{O} + ^{16}\text{O}$, but found that the dominant nuclear sensitivity of the black-hole mass-gap boundary comes from $^{12}\text{C}(\alpha, \gamma)^{16}\text{O}$. The triple-alpha reaction is also important because it produces ^{12}C during helium burning, while $^{12}\text{C}(\alpha, \gamma)^{16}\text{O}$ converts part of this carbon into ^{16}O . Thus the final carbon abundance is governed mainly by the competition between these two helium-burning reactions.

This conclusion was confirmed in [3] using updated stellar-evolution calculations: the lower edge of the mass gap changes strongly with the $^{12}\text{C}(\alpha, \gamma)^{16}\text{O}$ rate, whereas the later heavy-ion fusion rates $^{12}\text{C} + ^{12}\text{C}$, $^{12}\text{C} + ^{16}\text{O}$, and $^{16}\text{O} + ^{16}\text{O}$ move the boundary by only $\lesssim 1 M_{\odot}$. Therefore, for fixed stellar-evolution inputs, such as metallicity, mass loss, mixing, and the adopted triple- α and carbon-burning rates [1–3], the leading nuclear uncertainty is the $^{12}\text{C}(\alpha, \gamma)^{16}\text{O}$ rate, because it fixes the residual carbon abundance after core-helium burning.

Therefore, any inference that maps the observed black-hole mass distribution onto a value of $S(300 \text{ keV})$ must remain consistent with independent nuclear constraints on the $^{12}\text{C}(\alpha, \gamma)^{16}\text{O}$ reaction, including direct and indirect measurements, R -matrix extrapolations, and ANC constraints on the subthreshold and ground-state contributions.

In Ref. [3], $\sigma = 0$ corresponds to the adopted central value

$$S_0(300 \text{ keV}) = 140 \text{ keV b},$$

and one unit change in σ corresponds approximately to a variation of 20 keV b. Thus, the shifted value may be written as

$$S(300 \text{ keV}) \simeq S_0(300 \text{ keV}) + 20\sigma \text{ keV b}.$$

For example, the $\sigma = -1$ point corresponds approximately to

$$S(300 \text{ keV}) \simeq 120 \text{ keV b}.$$

The present ANC-constrained value,

$$S_{\text{tot}}(300 \text{ keV}) = 118 \text{ keV b},$$

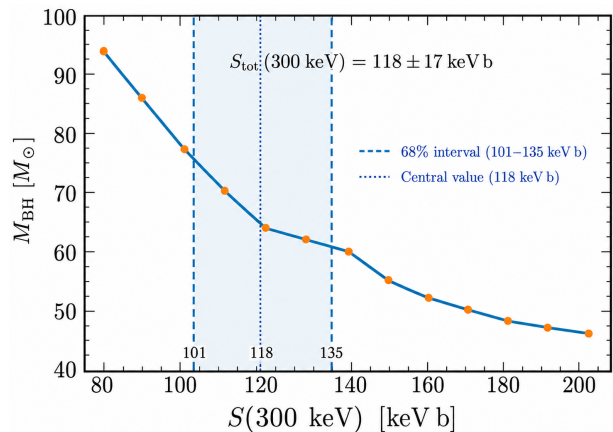


FIG. 5. Dependence of the maximum first-generation black-hole mass, identified with the lower edge of the pair-instability black-hole mass gap, on the astrophysical S factor $S(300 \text{ keV})$ for the $^{12}\text{C}(\alpha, \gamma)^{16}\text{O}$ reaction. The curve was redrawn from the lower-edge result of Ref. [3]. The original horizontal axis in Ref. [3] was expressed in terms of the reaction-rate variation parameter $\sigma[^{12}\text{C}(\alpha, \gamma)^{16}\text{O}]$. Here it is converted approximately to $S(300 \text{ keV})$, where $\sigma = 0$ corresponds to $S_0(300 \text{ keV}) = 140 \text{ keV b}$, and one unit change in σ corresponds approximately to 20 keV b. The figure illustrates the inverse trend: larger values of $S(300 \text{ keV})$ correspond to a smaller maximum first-generation black-hole mass and hence to a lower edge of the mass gap.

therefore corresponds to

$$\sigma \simeq -1.1.$$

Thus, the present ANC-constrained rate is very close to the $-\sigma$ rate inferred from Refs. [3, 8], differing from it by only about 2%.

To make this connection more transparent, we transformed the dependence shown in Ref. [3] from the reaction-rate variation parameter σ to an approximate dependence on $S(300 \text{ keV})$. This transformation allows the lower-edge black-hole mass M_{BH}/M_{\odot} to be displayed directly as a function of $S(300 \text{ keV})$, as shown in Fig. 5.

The resulting curve should be understood as an approximate reparametrization of the horizontal axis of Ref. [3], not as a new stellar-evolution calculation. Using this curve together with the $S(300 \text{ keV})$ interval obtained in Eq. (6), we infer the corresponding interval for the maximum first-generation black-hole mass, or equivalently the lower edge of the pair-instability mass gap,

$$\frac{M_{\text{BH}}}{M_{\odot}} \simeq 61\text{--}75. \quad (7)$$

The present ANC-constrained reaction rate was calculated from the total $S_{\text{tot}}(E)$ obtained in this work using the integration interval $0.01 \leq E \leq 2.0 \text{ MeV}$. The resulting thermonuclear reaction rate $N_A \langle \sigma v \rangle$ is shown in Fig. 6.

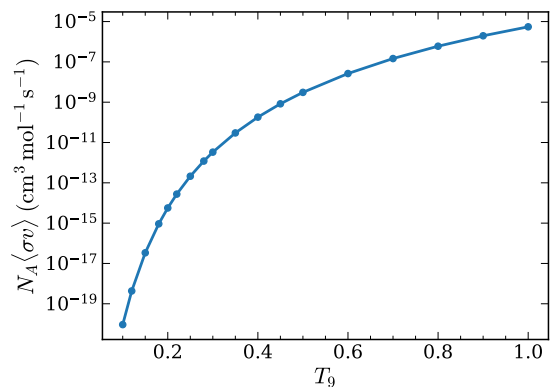


FIG. 6. Present ANC-constrained thermonuclear reaction rate $N_A\langle\sigma v\rangle$ for the $^{12}\text{C}(\alpha, \gamma)^{16}\text{O}$ reaction as a function of temperature T_9 , where T_9 is the temperature in units of 10^9 K.

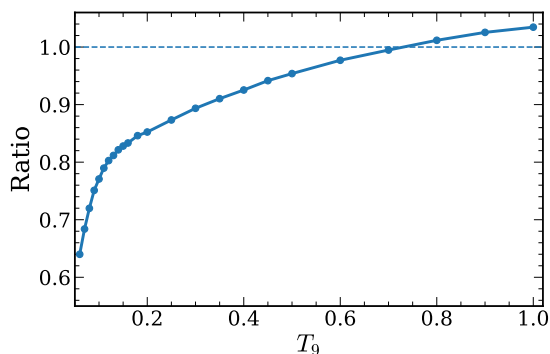


FIG. 7. Ratio of the present ANC-constrained thermonuclear reaction rate to the adopted rate from Table XXV of Ref. [8].

The ratio of the present rate to the adopted rate from Table XXV of Ref. [8] is shown in Fig. 7. At low temperatures, where the Gamow window lies in the sub-Coulomb region, the reaction rate is controlled mainly by the tails of the subthreshold states and therefore by the corresponding ANCs. In this region the ratio is close to the reduction expected from the S -factor ratio

$$\frac{S_{\text{present}}(300 \text{ keV})}{S_{\text{deBoer}}(300 \text{ keV})} = \frac{118}{140} \simeq 0.843. \quad (8)$$

Indeed, near the core-helium-burning temperature $T_9 \simeq 0.2$, the direct rate comparison gives

$$\frac{R_{\text{present}}}{R_{\text{deBoer}}} \simeq 0.85.$$

As the temperature increases, the Gamow window moves to higher energies, where the subthreshold tails are less dominant and the measured $S(E)$ data constrain the rate more strongly. Since both the present calculation and the deBoer evaluation describe the experimental data in this higher-energy region, the ratio gradually approaches unity.

VI. CONCLUSION

The central result of this work is that the extrapolated $^{12}\text{C}(\alpha, \gamma)^{16}\text{O}$ S factor at $E = 300$ keV must remain constrained by nuclear physics and cannot be determined solely from BH population arguments. The quantity $S(300 \text{ keV})$ is directly connected with the ANCs of the subthreshold and ground-state configurations, in particular C_1 , C_2 , and C_0 . By contrast, the lower edge of the black-hole mass gap is not directly measured; it is inferred indirectly from gravitational-wave population analyses and depends on assumptions about spin distributions, hierarchical mergers, selection effects, priors, and the adopted population model. Therefore, an astrophysical inference that requires values of $S(300 \text{ keV})$ outside the independently allowed nuclear-physics domain is not physically well constrained and is difficult to reconcile with independent nuclear constraints.

The available ANC information does not support very large values such as

$$S(300 \text{ keV}) \sim 240\text{--}263 \text{ keV b},$$

which appear in some interpretations based on a very low adopted mass-gap edge. Even values near $S(300 \text{ keV}) \simeq 170 \text{ keV b}$ are difficult to reconcile with present ground-state ANC constraints. In this work we therefore impose the independently determined ANC constraints from the outset. The subthreshold ANCs C_1 and C_2 are taken from sub-Coulomb transfer analyses, where the reaction is peripheral and the cross section is governed primarily by the relevant ANCs and the ^6Li ANC. The latter is independently constrained by six-body ab initio calculations and by the excellent agreement with the LUNA measurement of $\alpha + d \rightarrow ^6\text{Li} + \gamma$ [30]. For the ground-state ANC we use the modern range summarized in Table I, which favors $C_0 \gtrsim 600 \text{ fm}^{-1/2}$ and is incompatible with the very small ground-state ANC used in the older evaluation.

With these nuclear constraints imposed, the calculated total S factor is not an unconstrained fit to the measured total data. Rather, it is an ANC-constrained R -matrix extrapolation. The S_{E2} -only Bayesian analysis gives a posterior maximum near

$$C_0^{\text{MAP}} \simeq 703 \text{ fm}^{-1/2},$$

with a 68% credible interval

$$688 \leq C_0 \leq 798 \text{ fm}^{-1/2}.$$

This posterior does not support a drift toward small values of C_0 . The resulting total extrapolated value is

$$S_{\text{tot}}(300 \text{ keV}) \simeq 118 \text{ keV b}.$$

Propagating the ANC-driven uncertainty gives

$$S_{\text{tot}}(300 \text{ keV}) \simeq 116\text{--}122 \text{ keV b},$$

or equivalently

$$S_{\text{tot}}(300 \text{ keV}) = 118_{-2}^{+4} \text{ keV b},$$

where the quoted uncertainty reflects the propagated ANC uncertainty only. Additional systematic uncertainties associated with the R -matrix parametrization, channel radius, higher-lying levels, and experimental normalizations should be treated separately.

The measured total S -factor data alone do not uniquely determine $S_{\text{tot}}(300 \text{ keV})$. Different ANC choices can reproduce the measured energy region while leading to different low-energy extrapolations. Therefore, a Bayesian analysis based only on the total S -factor data is premature as a determination of $S_{\text{tot}}(300 \text{ keV})$. A physically meaningful Bayesian treatment should therefore propagate independently established ANC uncertainties rather than freely determining the ANCs from the present total-capture data alone.

Finally, using the transformed relation between the lower edge of the black-hole mass gap and $S(300 \text{ keV})$, based on Ref. [3], the present ANC-constrained range gives

$$\frac{M_{\text{BH}}}{M_{\odot}} \simeq 61\text{--}75.$$

This estimate is consistent with the mass-gap boundary inferred in Refs. [1–3], where a representative value $59_{-13}^{+34} M_{\odot}$ was obtained, and lies within that interval. It also overlaps with the interval $50\text{--}70 M_{\odot}$ [4].

Thus, the nuclear-physics constrained value of $S(300 \text{ keV})$ favors a relatively high lower edge of the first-generation black-hole mass gap. In particular, the present result does not support a strong downward shift of this boundary to $\sim 45 M_{\odot}$, which would require very large $S(300 \text{ keV})$ values. Agreement with gravitational-wave population observables alone is therefore insufficient; the inferred reaction rate must also remain consistent with independent nuclear-physics constraints.

-
- [1] R. Farmer, M. Renzo, S. E. de Mink, M. Fishbach, and S. Justham, *Astrophys. J. Lett.* **902**, L36 (2020). doi.org/10.3847/2041-8213/abbadd
- [2] S. E. Woosley and A. Heger, *Astrophys. J. Lett.* **912**, L31 (2021). doi.org/10.3847/2041-8213/abf2c4
- [3] A. K. Mehta, A. Buonanno, J. Gair, M. C. Miller, E. Farag, R. J. deBoer, M. Wiescher, and F. X. Timmes, *Astrophys. J.* **924**, 39 (2022). doi.org/10.3847/1538-4357/ac3130
- [4] Y.-Z. Wang, Y.-J. Li, S.-J. Gao, S.-P. Tang, and Y.-Z. Fan, arXiv:2510.22698 [astro-ph.HE]. doi.org/10.48550/arXiv.2510.22698
- [5] H. Tong *et al.*, arXiv:2511.05316 [astro-ph.HE]. doi.org/10.48550/arXiv.2511.05316
- [6] F. Antonini, I. M. Romero-Shaw, and T. Callister, *Phys. Rev. Lett.* **134**, 011401 (2025). doi.org/10.1103/PhysRevLett.134.011401
- [7] A. Ray and V. Kalogera, *Astrophys. J. Lett.* **998**, L20 (2025). doi.org/10.3847/2041-8213/ae374d
- [8] R. J. deBoer, J. Görres, M. Wiescher, R. E. Azuma, A. Best, C. R. Brune, C. E. Fields, S. Jones, M. Pignatari, K. Smith, *et al.*, *Rev. Mod. Phys.* **89**, 035007 (2017). doi.org/10.1103/RevModPhys.89.035007
- [9] R. Abbott, T. D. Abbott, S. Abraham, F. Acernese, K. Ackley, C. Adams, R. X. Adhikari, V. B. Adya, C. Affeldt, M. Agathos, *et al.*, *Phys. Rev. Lett.* **125**, 101102 (2020). doi.org/10.1103/PhysRevLett.125.101102
- [10] B. P. Abbott, R. Abbott, T. D. Abbott, S. Abraham, F. Acernese, K. Ackley, C. Adams, R. X. Adhikari, V. B. Adya, C. Affeldt, *et al.*, *Astrophys. J. Lett.* **900**, L13 (2020). doi.org/10.3847/2041-8213/aba493
- [11] G. R. Caughlan and W. A. Fowler, *At. Data Nucl. Data Tables* **40**, 283 (1988). doi.org/10.1016/0092-640X(88)90009-5
- [12] W. Xin *et al.*, *Res. Astron. Astrophys.* **26**, in press (2026).
- [13] A. M. Mukhamedzhanov, R. J. deBoer, B. F. Irgaziev, L. D. Blokhintsev, A. S. Kadyrov, and D. A. Savin, *Phys. Rev. C* **110**, 055803 (2024). doi.org/10.1103/PhysRevC.110.055803
- [14] A. M. Mukhamedzhanov, *Phys. Rev. C* **113**, 025803 (2026). doi.org/10.1103/PhysRevC.113.025803
- [15] C. R. Brune, W. H. Geist, R. W. Kavanagh, and K. D. Veal, *Phys. Rev. Lett.* **83**, 4025 (1999). doi.org/10.1103/PhysRevLett.83.4025
- [16] M. L. Avila, G. V. Rogachev, E. Koshchiy, L. T. Baby, J. Belarge, K. W. Kemper, A. N. Kuchera, E. Uberseder, and D. Santiago-Gonzalez, *Phys. Rev. Lett.* **114**, 071101 (2015). doi.org/10.1103/PhysRevLett.114.071101
- [17] L. D. Blokhintsev, V. I. Kukulkin, A. A. Sakharuk, D. A. Savin, and E. V. Kuznetsova, *Phys. Rev. C* **48**, 2390 (1993). doi.org/10.1103/PhysRevC.48.2390
- [18] C. Hebborn, M. L. Avila, K. Kravvaris, G. Potel, and S. Quaglioni, *Phys. Rev. C* **109**, L061601 (2024). doi.org/10.1103/PhysRevC.109.L061601
- [19] L. D. Blokhintsev, A. S. Kadyrov, A. M. Mukhamedzhanov, and D. A. Savin, *Eur. Phys. J. A* **59**, 162 (2023). doi.org/10.1140/epja/s10050-023-01091-5
- [20] M. Assunção, M. Fey, A. Lefebvre-Schuhl, J. Kiener, V. Tatischeff, J. W. Hammer, C. Beck, C. Boukari-Pelissie, A. Coc, J. J. Correia, *et al.*, *Phys. Rev. C* **73**, 055801 (2006). doi.org/10.1103/PhysRevC.73.055801
- [21] M. C. Morais and R. Lichtenthäler, *Nucl. Phys. A* **857**, 1 (2011). doi.org/10.1016/j.nuclphysa.2011.03.005
- [22] K. Kundalia *et al.*, *Phys. Lett. B* **869**, 139836 (2025). doi.org/10.1016/j.physletb.2025.139836
- [23] D. B. Sayre, C. R. Brune, D. E. Carter, D. K. Jacobs, T. N. Massey, and J. E. O'Donnell, *Phys. Rev. Lett.* **109**, 142501 (2012). doi.org/10.1103/PhysRevLett.109.142501
- [24] L. H. Chien and P. Descouvemont, *Phys. Rev. C* **110**, 024611 (2024). doi.org/10.1103/PhysRevC.110.024611
- [25] S. Adhikari *et al.*, *J. Phys. G* **44**, 015102 (2017). doi.org/10.1088/0954-3899/44/1/015102

- [26] L. D. Blokhintsev and D. A. Savin, Phys. Atom. Nucl. **89**, in press (2026).
- [27] Y. Shen, B. Guo, R. J. deBoer, E. Li, *et al.*, Astrophys. J. **945**, 41 (2023). doi.org/10.3847/1538-4357/acb7de
- [28] D. Schürmann, L. Gialanella, R. Kunz, and F. Strieder, Phys. Lett. B **711**, 35 (2012). doi.org/10.1016/j.physletb.2012.03.064
- [29] H. Yamaguchi, K. Sagara, K. Fujita, D. Kodama, Y. Narikiyo, K. Hamamoto, T. Ban, N. Tao, and T. Teranishi, AIP Conf. Proc. **1594**, 229 (2014). doi.org/10.1063/1.4874074
- [30] M. Anders *et al.* (LUNA Collaboration), Phys. Rev. Lett. **113**, 042501 (2014). doi.org/10.1103/PhysRevLett.113.042501